Interpolation of Operational Radar Data to a Regular Cartesian Grid Exemplified by Munich's Airport Radar Configuration

AYLA AUGST AND MARTIN HAGEN

Institut of Atmospheric Physics, DLR, Oberpfaffenhofen, Germany

ABSTRACT

Two methods for avoiding errors in the interpolation of operational radar data to a regular grid are presented. The issue is the interpolation of radial velocity and the subsequent estimation of horizontal wind components. It is shown how a vertical gradient of the horizontal wind in combination with gaps of data between scans with different elevation angles affect the interpolation. Simulated radar data for the radar configuration covering the Munich airport in southern Germany are used for illustration. The origin of the abovementioned errors is explained using simplified wind fields. With wind fields generated by the German nonhydrostatic atmospheric prediction model COSMO-DE, the effectiveness of the methods is presented. Both methods contribute to a reduction in interpolation error—by 44% and 35%, respectively—compared to a standard interpolation scheme used for many operational radar configurations.

1. Introduction

Many studies have proven that the knowledge of the three-dimensional wind vector is of great importance for various kinds of atmospheric topics, from diagnostic research of wind and weather systems (e.g., Van Zadelhoff et al. 2014), as well as transport processes in the atmosphere (e.g., Woodhouse et al. 2013), to nowcasting and numerical forecasting (e.g., Simonin et al. 2014). For all of these disciplines, the 3D wind field is directly—or at least indirectly—of interest.

Since Probert-Jones (1960) showed the potential of using radars to measure horizontal winds, many different methods have been developed to generate a 3D wind vector from the measured radial velocities. Starting with a single-Doppler radar to measure radial wind and reflectivity within a volume, methods like velocity–azimuth display (VAD) (Lhermitte (1966), volume velocity processing (VVP) (Waldteufel and Corbin 1979; Easterbrook 1975), and echo tracking (see, e.g., Tuttle and Foote 1990) have been developed and proven many times.

When using two or more Doppler radars measuring the same volume from various directions, the horizontal wind vector can be calculated directly with the use of dual- and multiple-Doppler techniques (Armijo 1969;

Miller and Strauch 1974). As the contribution from the vertical wind component w to the measured Doppler velocity is small due to the low elevation angles (Laroche and Zawadzki 1994; Protat and Zawadzki 1999), calculating w directly leads to large errors. Given the horizontal wind components u and v and an estimate of the particle fall velocity (Armijo 1969), w can be calculated by either integrating the mass continuity equation (Protat and Zawadzki 1999; Ray et al. 1980; Miller and Strauch 1974) or minimizing a cost function within a 3D variational analysis (Gao et al. 1999; Nash and Sofer 1996).

Radars measure in spherical coordinates (see Fig. 1). Therefore, irrespective of what kind of analysis is used to determine the 3D wind field, a step within the calculation has to be the direct or indirect interpolation of the radar data to a regular grid—for example, a Cartesian grid—which can be a great source of error. In that context, direct means the radar measurements are interpolated in a first step before the calculation of the three wind components. Indirect means the radar measurements are included within a minimization process with a weighting function depending on the distance to the Cartesian grid points, as shown in Bousquet and Chong (1998).

Compared to the long history of using radars to measure wind or rainfall in field experiments, the coverage with operational weather radars has only recently been extended. Radars that run for operational purpose

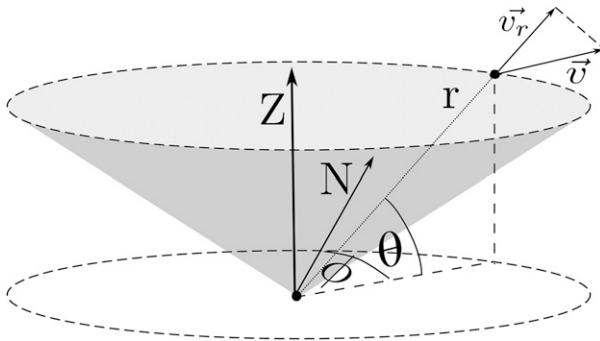*Corresponding author e-mail*: Ayla Augst, ayla.augst@dlr.de

FIG. 1. Conical measurement geometry of ground-based weather radars. Radars measure the radial component v_r of the wind vector **v** in spherical coordinates with elevation angle θ, azimuth angle ϕ, and distance r.

produce scans of a whole volume within a short time. Therefore, the number of elevation angles are reduced to a minimum (e.g., for systems of the German radar network, about 10 elevation angles up to 20°; see Fig. 2), which leads to a lack of data coverage increasing with altitude, respectively with distance to the radar. Methods designed to interpolate dense radar data as present in field experiments are not always suitable for interpolating sparse data as well. Especially in combination with a gradient in wind (mainly a gradient in the vertical, as the sampling rate in the horizontal is usually high due to small elevation angles and short bin sizes), a lack of data can lead to errors in interpolation.

Since the analysis with operational radar data is quite young, as already pointed out by Bousquet et al. (2016), there exist only a small amount of publications that deal with the finding of an optimal interpolation scheme

depending on the radar geometry and scanning strategy (e.g., Zhang et al. 2005; Lakshmanan et al. 2006). These publications consider the interpolation of reflectivity data rather than wind.

In this paper, a method is presented to deal with the challenge of interpolating wind data from operationally used radars. This is unique, as differences in the field characteristics of wind and precipitation lead to different needs for the interpolation. The radar network is exemplified by the radar configuration covering the Munich airport in southern Germany. The Munich airport is covered by three radars that can be used to estimate the wind field.

The paper is structured as follows. Section 2 gives an overview of the radar configuration and the synthetic wind fields, which are used to generate synthetic radial velocities. In section 3a the source of the described interpolation errors is explained in more detail, followed by the interpolation methods that are used for this work with idealized wind fields (section 3b). In the subsequent section (section 3c), the developed methods are applied to more realistic wind fields from a mesoscale model output. A brief summary and conclusions are given in section 4.

2. Database

As mentioned above, the existing radar configuration that covers the Munich airport is used to generate simulated radar data.

Figure 3 presents the location of the radars with respect to the analyzed volume ($100 \times 100 \times 10 \, \text{km}^3$), which is defined from 47.97° to 48.71°N latitude, from
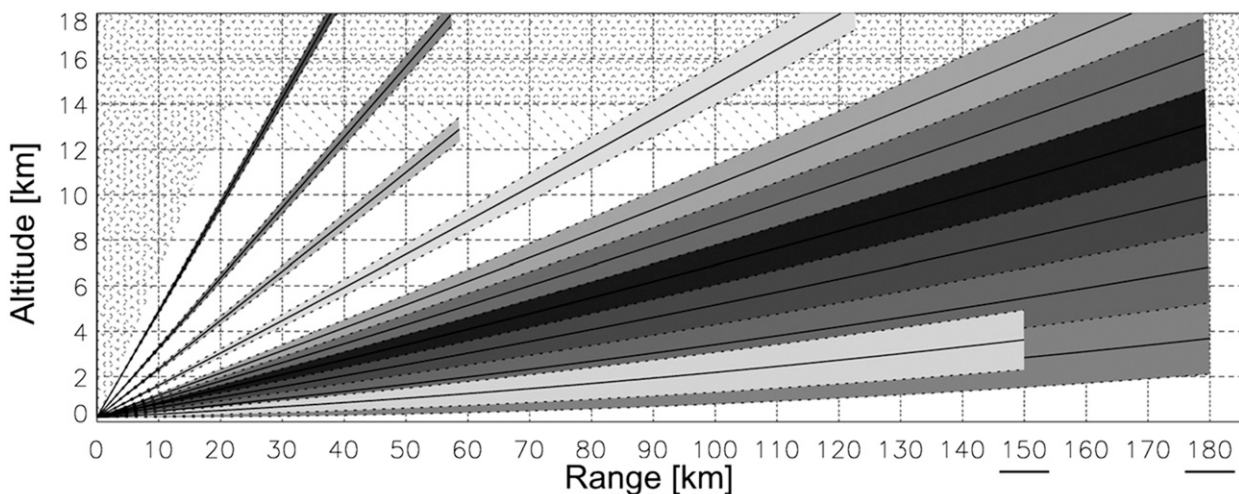

FIG. 2. Scan strategy of ground-based weather radars of the German radar network. One volume scan consists of 10 elevation angles from 0.5° to 25° and an additional precipitation scan at 0.8° within 5 min (cf. Helmert et al. 2014).
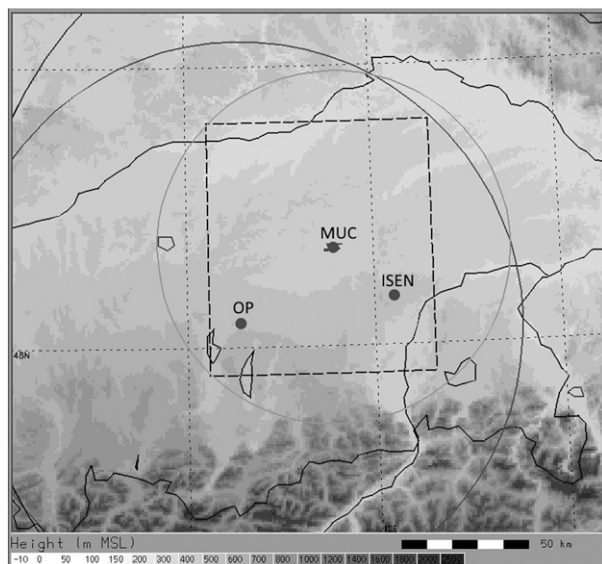
FIG. 3. Radar configuration in the area around the Munich airport. MUC: radar at the Munich airport (max range 75 km); OP: radar of the Deutsches Zentrum für Luft- und Raumfahrt (DLR; German Aerospace Center) in Oberpfaffenhofen, POLDIRAD (max range 120 km); and ISEN: radar of the DWD in Isen (max range 180 km).

$11.12°$ to $12.32°E$ longitude, and from 0.5 to 10.5 km MSL. The grid spacing is 1 km in each direction. The ground level of the terrain rises from about 400 m MSL in the north to 700 m in the south. The radars have maximum ranges from 75 to 180 km and 10–11 different elevation angles.

For the simulation of synthetic radar data, the location of the radars, the maximum range, and the bin size are equal to the existing radar geometries. For all data elevation angles up to $20°$ with the spacing of the operational scan mode of the radars and the full set of azimuth angles (see Table 1 for more details) are used. Different beamwidths are not considered. The beamwidth is assumed to be $1°$.

To explain the difficulty in the interpolation, simplified wind fields are used to generate simulated radar measurements. These wind fields are directed to the east with a mean wind speed of $20\,\mathrm{m\,s^{-1}}$ and a vertical gradient

at different heights of 2–$10\,\mathrm{m\,s^{-1}\,km^{-1}}$. For these wind fields, the full possible data coverage is assumed and no measurement error is added.

For the test with more realistic cases, 16 wind fields are used, generated by the German COSMO-DE Model, which is a nonhydrostatic atmospheric prediction model that has been developed by the German Weather Service (DWD). The model grid spacing of 2.8 km is bilinearly interpolated to fit the analysis grid with a grid spacing of 1 km in each direction. For a more detailed description of the COSMO-DE Model, see Baldauf et al. (2011).

Besides horizontal and vertical wind components, prognostic variables are an estimate of the specific water content of rain, snow, and graupel. The sum of specific water constant W is used to calculate an estimation of measured radar reflectivity Z with the equation $W = qZ^{4.7}$ proposed by Kessler (1995). The value of $q = 5.4$ was determined empirically.

At first the simulated radial velocity data without any restriction or added error is used. Afterward, with the generated radar reflectivity, the areas of data coverage are limited to those where radar reflectivity is greater than $-20\,\mathrm{dB}Z$ and a normal distributed random error with a standard deviation of $\sigma = 1\,\mathrm{m\,s^{-1}}$ is added to the simulated Doppler velocity data, which is in the order of radar measurement uncertainty. Furthermore, an estimated particle fall velocity depending on the calculated reflectivity has been added to the data. To simulate a radar data preprocessing step, each scan is projected onto a Cartesian grid of $100 \times 100\,\mathrm{km^2}$ with a grid resolution of 0.5 km in both horizontal directions and a 2.5×2.5-$\mathrm{km^2}$ median filter is applied.

Figure 4 shows the mean percentage of grid coverage for the horizontal plane at different altitude levels to get a better insight of the data coverage in the whole volume in the case of full data coverage (simulated radial velocity data without any restriction) and limited data coverage (simulated radial velocity data limited according to simulated reflectivity values). For interpolation, the radius of influence—that is, the maximum distance that a data point can have to a grid point

TABLE 1. Scan geometries of radars covering the Munich airport.

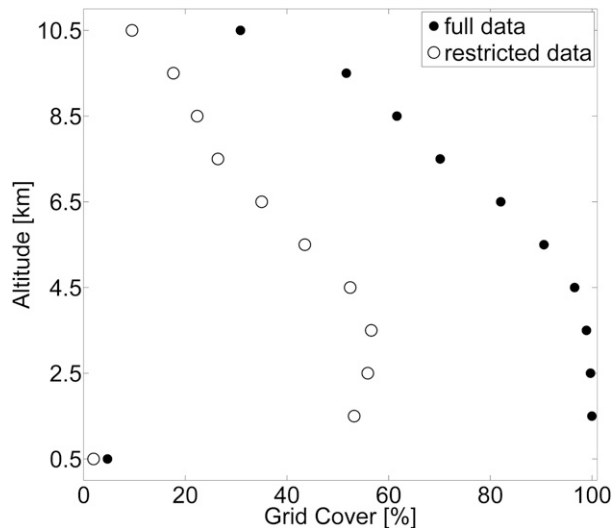| System	OP	ISEN	MUC
Wavelength (cm)	5.5	5.3	3.2
Beamwidth (°)	1.0	1.0	1.2
Range (km)	120	180	75
Range resolution (m)	150	100	150
Elevations used (°)	1.0, 2.0, 3.5, 5.0, 7.0, 9.0, 11.0, 13.0, 15.0, 17.0, and 20.0	0.5, 1.5, 2.5, 3.5, 4.5, 5.5, 8.0, 12.0, and 17.0	1.0, 2.0, 3.0, 4.5, 6.0, 8.0, 12.0, and 20.0

FIG. 4. Mean grid coverage of radar data (%) for interpolation to 10 altitude levels. The horizontal radius of influence is set to 3 km. In the case of full data coverage (e.g., large area stratiform rain) up to an altitude of 4 km above ground, data are available at almost every grid point. For the data that are restricted to areas where rain is expected, the maximum data coverage is reached at 3 km above ground on average, with a coverage of less than 60%.
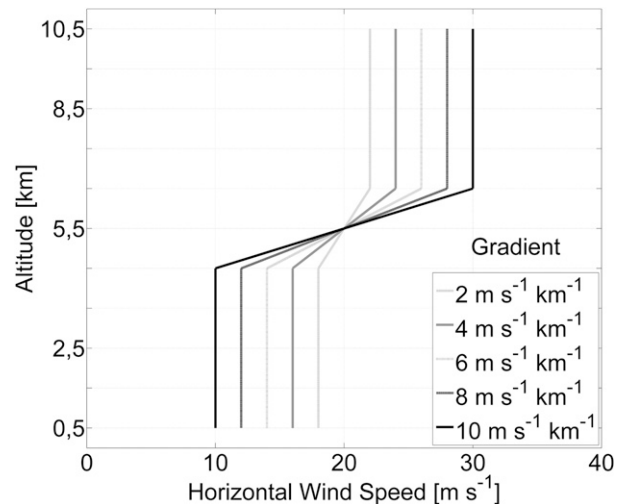

FIG. 5. Schematic plot of wind speeds for the idealized wind fields. Five different vertical gradients centered at an altitude level of 5.5 km MSL are shown.

to have an impact on it—in the horizontal, is set to 3 km. In the vertical the radius of influence depends on the range, as the beamwidth increases with the range, due to the beam broadening of about 1°. This is an established radius of influence for interpolation of radar data, for example, used within various analyses with the French operational radar network (see, e.g., Bousquet and Tabary 2014; Beck et al. 2014).

Analyzed wind fields

The idealized wind fields have simplified structures. They have only horizontal wind components to the east. Terms w and v are set to zero in all cases. To illustrate an increasing interpolation error with increasing vertical gradient of the horizontal wind field, we generated 5×11 different wind fields according to five different vertical gradients (2, 4, 6, 8, and $10\,\mathrm{m\,s^{-1}\,km^{-1}}$) centered at each of the 11 altitude levels (0.5, ... , 10.5 km MSL). The vertical gradient can be found over three altitude level and is zero elsewhere. For an altitude of 5.5 km, a schematic plot of the five different wind fields can be seen in Fig. 5. The centered wind speed is always set to $20\,\mathrm{m\,s^{-1}}$.

For more realistic situations, 16 different wind fields from analyses of the COSMO-DE Model are used. The corresponding weather situations had more or less stratiform rainfall to ensure that there is enough data to have significant results, even in the case of restricted data coverage. Some information about vertical wind

speed and vertical wind gradient are summarized in appendix A (Tables A1 and A2; Figs. A1–A4) to get a better understanding of the analyzed wind fields.

3. Methodology

Hereinafter the methods to interpolate radar measurements to a Cartesian grid are presented. The first part (section 3a) describes the general method of interpolation and errors that occur due to the measurement geometry, especially in the case of a strong vertical gradient of the wind field. The second part (section 3b) shows how the radius of influence affects the interpolation error. In the last part (section 3c), a method is presented to include strong vertical gradients in the interpolation to minimize its contribution to the interpolation error.

a. Interpolation to a Cartesian grid

The radar data considered are collected at points defined by an azimuth angle, an elevation angle, and the distance. This is inappropriate for retrieving and analyzing a wind field. Therefore, the data have to be interpolated to a regular grid, for example, a Cartesian grid.

For the interpolation of data to grid points of a predefined grid, every data point is interpolated with an appropriate weight to all grid points that are located within the radius of influence. The weight is a function of the distance to the grid point. In the case of different data sources or additional information about data quality, the weight can also be a function of the data quality. For merging multiple radar data, additional weights can be considered. Lakshmanan et al. (2006) considered a weight

decreasing with increasing range to incorporate beam spreading. Moreover, a common analysis time has to be set and a weight depending on the time difference between analysis and measurement can be applied.

As for the simulation of radar data for this paper, the scan time is not considered; the weight for each observation i is simplified in the following way:

$$w_i = w_{\text{hor}} \times w_{\text{vert}} \times w_{\text{el}}$$

$$w_{\text{hor}} = \frac{R_{\text{hor}}^2 - r_{i,\text{hor}}^2}{R_{\text{hor}}^2 + R_{i,\text{hor}}^2}, \quad \text{for} \quad R_{i,\text{hor}}^2 \leq R_{\text{hor}}^2$$

$$w_{\text{vert}} = e^{-(1/2)(r_{i,\text{vert}}/\sigma_i)^2}, \quad \text{for} \quad R_{i,\text{vert}}^2 \leq R_{\text{vert}}^2$$

$$w_{\text{el}} = \left(1 - \frac{\theta}{90°}\right).$$

Here, R_{hor} and R_{vert} are the horizontal and vertical radius of influence, respectively; $r_{i,\text{hor}}$ and $r_{i,\text{vert}}$ are the horizontal and vertical distances between the observation and the grid point, respectively; and w_{hor} is a Cressman weighting function (Cressman 1959), whereas w_{vert} is a Gaussian weighting function with σ_i set so that w_{vert} is less than 0.01 for $r_{i,\text{vert}} \geq R_{\text{vert}}$. In the vertical a different weighting function is used to give measurements that differ in the vertical direction even less influence. Instead of using two different weighting functions, an option to implement a direction splitting is—for example, the A–B filter—proposed by Askelson et al. (2000), which provides direction splitting and an automatic adaption to data density.

The quantity θ is the elevation angle of the beam. A weight depending on the elevation angle of the beam is included to the weighting function for two reasons. First, the radial velocity is corrected with an estimation of the particle fall velocity. Since little is known about the particle's size and nature, the advice of Miller and Strauch (1974) is followed and the empirical relationship of Joss and Waldvogel (1970) to estimate the particle fall velocity is used. They observed seven different precipitation situations and defined fall velocities by eye. Nevertheless, the empirical estimation of the particle fall velocity can be very imprecise: The greater the elevation angle, the more influence the particle fall velocity has on the measured radial velocity. Therefore, measurements with a great elevation angle have less weight to the calculation of the velocity. Second, the vertical wind component of the radial velocity is neglected in the analysis, since in general for low elevation angles, as used for operational radar, w contributes little [$\sin(\theta) \times w$] to the radial velocity (Laroche and Zawadzki 1994; Protat and Zawadzki 1999).

The positions of the observations are calculated with their elevation angle, azimuth angle, range, and location of the radar with respect to the grid. For each grid point, an ellipsoid is defined. Each observation that lies within this ellipsoid is influenced by the wind vector calculated for that grid point. The ellipsoid is defined by two different radii: R_{hor} in the horizontal direction and R_{vert} in the vertical direction. The calculation of the wind vector at one grid point is done using a weighted-least-squares fit of all measurements that fall within the radius of influence of this point. The target function for this fit is defined as

$$F(\mathbf{v}_p) = \sum_{i=1}^{N} (\mathbf{n}_i \cdot \mathbf{v}_{p,i} - \mathbf{v}_{r,i})^2 / \sigma_i^2, \tag{1}$$

where $\mathbf{v}_{r,i}$ is the radial velocity and $\mathbf{v}_{p,i}$ is the particle velocity vector $(u,v)^{\text{T}}$ in two horizontal directions. The $\mathbf{n}_i$ is a unit vector pointing in the direction of the radar beam, N is the number of observations that are included, and $\sigma_i = \sigma_0^2 / w_i$ is the variance of each observation with σ_0^2 representing the error associated with the measurement. We assume σ_0^2 to be $1 \, \text{m s}^{-1}$ irrespective of the measurement. In general additional information can be used to set a value for σ_0^2, for example, a signal-to-noise ratio.

Minimizing $F(\mathbf{v}_p)$ with respect to u and v leads to a system of linear equations with the following form:

$$\begin{pmatrix} a_{\text{xx}} & a_{\text{xy}} \\ a_{\text{yx}} & a_{\text{yy}} \end{pmatrix} \begin{pmatrix} u \\ v \end{pmatrix} = \begin{pmatrix} b_x \\ b_y \end{pmatrix}, \quad \text{with} \tag{2}$$

$$a_{\text{xx}} = \sum_i [\cos(\theta)\sin(\phi)]^2 w_i$$

$$a_{\text{xy}} = \sum_i [\cos(\theta)\sin(\phi)][\cos(\theta)\cos(\phi)]w_i = a_{\text{yx}}$$

$$a_{\text{yy}} = \sum_i [\cos(\theta)\cos(\phi)]^2 w_i$$

$$b_x = \sum_i [\cos(\theta)\sin(\phi)]v_{r,i}w_i$$

$$b_y = \sum_i [\cos(\theta)\cos(\phi)]v_{r,i}w_i.$$

Here $\mathbf{v}_{r,i}$ is the observed radial velocity, θ is the elevation angle of the beam, and ϕ is the azimuth angle.

To solve Eq. (2) the system matrix $\mathbf{A}$ on the left side is diagonalized, following López Carrillo and Raymond (2011), such that the entries of the 2×2 matrix $\mathbf{D_A} = \mathbf{R}^{\text{T}} \mathbf{A} \mathbf{R}$ are the eigenvalues of $\mathbf{A}$. With the orthogonal transformation $\mathbf{R}$ a velocity vector $\mathbf{U}$ is found, such that $\mathbf{v}_p = \mathbf{R}\mathbf{U}$. The velocities are defined in a rotated reference frame, where they can be estimated independent of each other. This is very useful in case there is not enough information to determine both components—just one of them is uncertain. For each grid point, this new reference frame is defined by
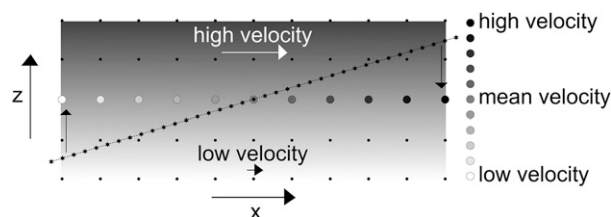
FIG. 6. Radar beam (dotted line of asterisks) propagating through a region of strong vertical wind gradient. Dark shading indicates high horizontal wind speed; light shading indicates low horizontal wind speed. Equidistant black dots in the background are the grid points of the interpolation grid. The radar measurements (asterisks along the beam) are interpolated to the horizontal grid at the mean altitude level.

two eigenvectors and the corresponding eigenvalues. The error associated with each component of the velocity is defined as the reciprocal of the square root of the eigenvalue:

$$\sigma_{\alpha} = 1/\sqrt{a_{\alpha}}. \qquad (3)$$

Here a_{α} is the eigenvalue associated with the component α. The eigenvalues can be used as a quality parameter for including and excluding data points in the analysis.

A detailed description of the overall formalism can be found in López Carrillo and Raymond (2011). It should be noted that they also consider the vertical direction in the minimization process unlike us. The vertical component can be later estimated with the use of the mass continuity equation as in Protat and Zawadzki (1999), Ray et al. (1980), and Miller and Strauch (1974).

The weighted least squares fit ensures that measurements at larger distances from the grid point or with large uncertainties contribute less than closer and more confident measurements. Although a least squares fit is not robust against outliers, it works well in the case of dense data points. However, when operational radars run with a reduced number of elevation angles to save time, they produce a lack of data coverage increasing with altitude (see Fig. 2). Especially in combination with a strong vertical gradient of the wind vector, errors are produced in the interpolation.

Figure 6 shows a schematic plot of a radar beam (dotted line of stars) propagating through a region of strong vertical wind gradient within the analyzed volume, where dark gray indicates a high wind speed and white indicates a low wind speed. The defined Cartesian grid is plotted with equidistant black dots. The medium level is color coded with the schematic wind speed that is interpolated to that grid point, with an assumed vertical radius of influence of about one or two grid points and a horizontal radius of influence of about six or seven grid points. Each data point

(pictured as a star) is weighted with the distance to the grid points, but as there is information coming from only one beam and no information coming from a second beam above or below the other beam, grid points on the left side get more information from the region with low wind speed, whereas grid points on the right side get more information from the region with high wind speed. The resulting interpolated wind speed at the mean altitude shows a horizontal wind gradient, which does not exist in the original data, as the result of a projection of the vertical gradient. Giving a data point with a large distance to the grid point a small weight cannot compensate for too little information coming from an altitude level above or below this point.

To demonstrate how the interpolation error increases with increasing vertical gradient, simulated radar measurements from simplified wind fields are generated. The structure of these wind fields is explained in section 2b and summed up in appendix A. Ten wind fields with different vertical gradients from 1 to $10 \, \mathrm{m \, s^{-1}}$ within 1 km are used.

In the following analyses, all grid points where the number of simulated observations used in the least squares fit of the data is less than 25 or the first eigenvalue (the smaller eigenvalue, as they are sorted by size) is smaller than 0.015 are excluded to eliminate potential bad values. The improvement due to different interpolation methods is always given in percentage compared to the reference case (interpolation with a fixed interpolation radius).

Figure 7 shows contour plots of the interpolated wind field at an altitude level of 5.5 km for a vertical wind gradient of 1 (Fig. 7, left panel) and $5 \, \mathrm{m \, s^{-1} \, km^{-1}}$ (Fig. 7, middle panel), and a plot of the relative root-mean-square error (RMSE) over the increasing vertical wind gradient at the same altitude level (Fig. 7, right panel). The true wind speed at this altitude level is $20 \, \mathrm{m \, s^{-1}}$ at all grid points. White areas are not included in the evaluation, as there are not enough data or the first eigenvalue is smaller than 0.015, as explained above. The ring structure visible in the interpolation plots becomes stronger and the interpolation error increases with increasing gradient. For this analysis the interpolation is done using the operational scan geometry of the three radars (see Table 1).

Figure 8 shows a contour plot for similar conditions as in Fig. 7 (middle panel) with a vertical wind gradient of $5 \, \mathrm{m \, s^{-1} \, km^{-1}}$ but with the use of 20 elevation angles from 1° to 20° with a step of 1° instead of the operationally used scan mode.

There are examples showing that increasing interpolation error arises from a lack of data caused by the
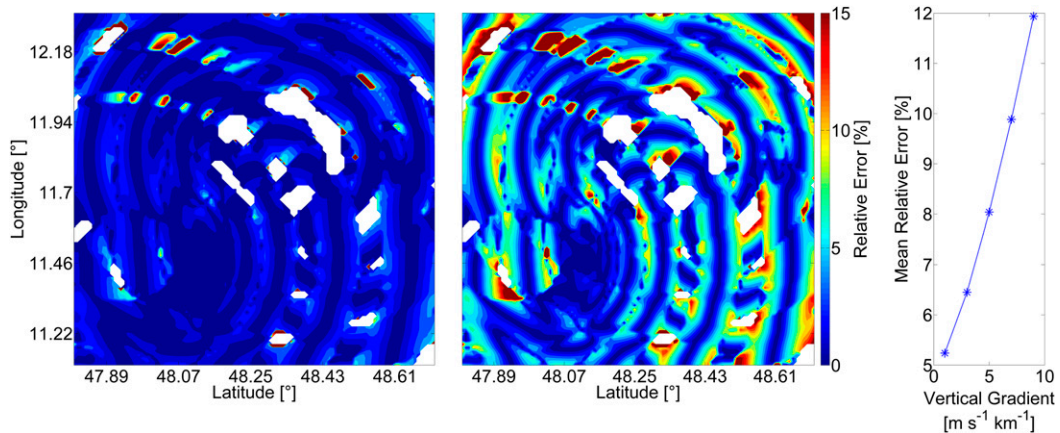
FIG. 7. Interpolated horizontal wind fields at an altitude of 5.5 km MSL. (left) The original wind field with a vertical gradient of a horizontal wind speed of $1 \, \mathrm{m \, s^{-1} \, km^{-1}}$. (middle) The original wind field with a vertical gradient of $5 \, \mathrm{m \, s^{-1} \, km^{-1}}$. (right) The RMSE at the same altitude level as a function of the vertical wind gradient.

scan strategy of operational radars. The mean interpolation error with the use of 20 elevation angles is reduced by 58.9% compared to the error when the number of elevation angles used operationally —that is, 9–10— are used depending on the radar. For all plots a horizontal interpolation radius of 3 km and a vertical interpolation radius as a function of the radar beamwidth [$R_{\mathrm{vert}} = r\tan(\frac{1}{2}\beta)$] is used, where β is the radar beamwidth and r is the distance of the data point to the radar. It is worth noting that the determination of the vertical radius of influence is a special task that must be treated carefully. With a vertical radius of influence of half the beamwidth, we get the best results. A more detailed description is given at the end of section 3b.

b. Optimal radius of influence

The error of the interpolation in the presence of a vertical wind gradient increases with decreasing data coverage. Therefore, the radius of influence for interpolating a data point to the grid is of importance and should be selected according to the given radar configuration. As shown in section 3a, a horizontal radius of influence of 3 km and a vertical radius depending on the radar beamwidth—as it is used, for example, in an analysis with the French radar network (see, e.g., Bousquet et al. 2016; Bousquet and Chong 1998)—in the presented radar configuration can produce large errors in the case of stronger vertical wind gradients.

To overcome the handicap of a shortage in data, the horizontal radius of influence could be adjusted so that the radii of different beams overlap. A disadvantage of this is that small-scale features cannot be resolved anymore. Another possibility is to scale down the interpolation radius in the vertical so that the horizontal projection

of the vertical wind gradient is minimized. However, this leads to a great loss in the number of data points that can be used within the analysis.

An optimal radius of influence, depending on the lack of data (on the altitude level) and depending on the vertical wind gradient, can be found. Therefore, synthetic radar measurements out of 5×11 idealized wind fields are generated. These wind fields have vertical wind gradients of 2–$10 \, \mathrm{m \, s^{-1} \, km^{-1}}$ at 11 different altitude levels (0.5–10.5 km). Again, these synthetic measurements are produced with the geometry and scan strategy of the three radars described in section 2, are not restricted to areas of potential rainfall, and do not have errors. The synthetic measurements are
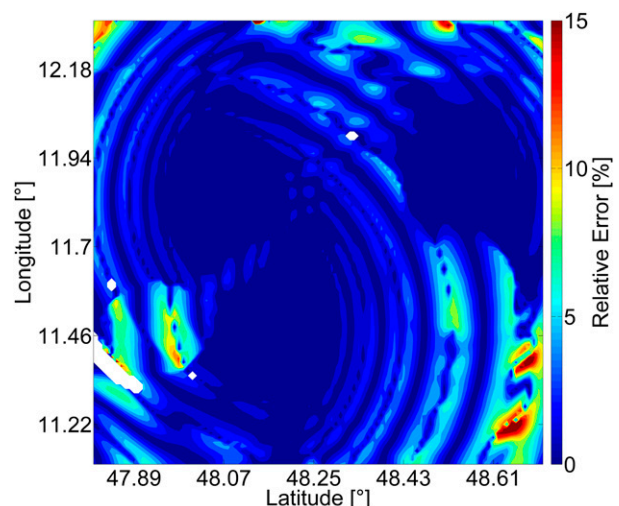

FIG. 8. Interpolated wind field at an altitude of 5.5 km MSL with a vertical gradient of a horizontal wind speed of $5 \, \mathrm{m \, s^{-1} \, km^{-1}}$. As in Fig. 7 (right panel), but with the use of 20 elevation angles from 1° to 20°.
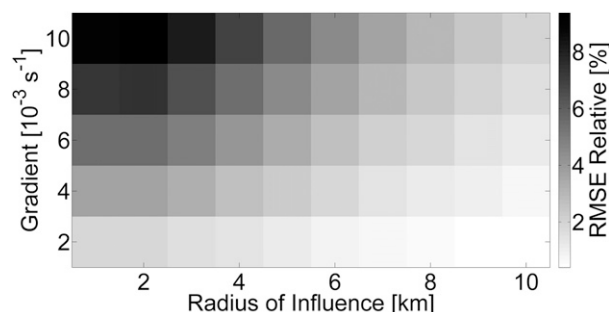
FIG. 9. RMSE as a function of the vertical wind gradient ($m\,s^{-1}\,km^{-1}$) and the radius of influence (km) 5.5 km.

interpolated to the defined grid with the use of 10 different horizontal radii of influence (1–10 km). The vertical radius of influence in all analyses is set as a function of beamwidth and distance to the radar (see section 3a) but with a minimum of 200 m.

Figure 9 shows the mean RMSE as a function of the vertical wind gradient ($m\,s^{-1}\,km^{-1}$) and the horizontal radius of influence (km) for an altitude level of 5.5 km. As can be seen, the error decreases continuously with increasing radius of influence in all cases. The mean error increases with increasing vertical wind gradient.

To find the optimal radius of influence as a function of vertical wind gradient and altitude level, all $5 \times 11 \times 10$ interpolated wind fields are analyzed and a lookup table is created (see Table B1). The lookup table contains the optimal radius of influence depending on the altitude level and the assumed vertical gradient. To find a balance between smoothing and error reduction, an optimal radius is found, as the radius for the interpolation mean absolute error is less than $0.5\,m\,s^{-1}$ for the first time.

For the evaluation of the improvement of using a variable radius of influence in different wind situations rather than a fixed radius of 3 km, synthetic observations for the three radars are generated out of 16 realistic wind fields from the output of the COSMO-DE Model (see section 2), again without error and with full coverage.

Figure 10 shows the resulting interpolation of one of the wind fields at an altitude level of 5.5 km MSL. Plotted is the horizontal wind speed $\mathbf{v} = (u^2 + v^2)^{1/2}$, where u and v are the two horizontal wind components. The original wind field (Fig. 10a) is the COSMO-DE analysis of the wind field in the domain of interest, 1130 UTC 17 January 2014. The horizontal wind speed ranges from 21 to $30\,m\,s^{-1}$ with a strong vertical gradient of about $7\,m\,s^{-1}\,km^{-1}$ on average and $14\,m\,s^{-1}\,km^{-1}$ for the peak. With the fixed horizontal influence radius of 3 km, a strong circular structure arises (Fig. 10b). This

structure is caused by the strong vertical gradient that is projected onto the horizontal due to small data coverage. Again, white areas are not included in the evaluation due to bad data coverage.

The variable radius of influence depends on the altitude and the estimated vertical gradient. From the lookup table we find this influence radius to be 8 km, as the mean vertical gradient of the horizontal wind speed is found to be $7\,m\,s^{-1}\,km^{-1}$ (see Table B1). For operational usage the vertical gradient can be estimated from the previous analysis or from model output.

As can be seen in Fig. 10c, the mean absolute error (MAE) is reduced in the case of the variable radius of influence (MAE = $0.57\,m\,s^{-1}$ compared to MAE = $0.93\,m\,s^{-1}$ for the reference case with a radius of influence of 3 km).

Figure 11a shows the RMSE and the MAE for all analyzed cases at altitude levels from 0.5 to $10.5\,m\,s^{-1}$, and for a fixed horizontal radius of influence of 3 km (black line) and a variable horizontal radius of influence depending on the vertical wind gradient and current altitude level (gray line). The plot clearly shows that the variable radius of influence reduces the mean RMSE by 44.9% and the MAE by 38.7% compared to the mean error with a fixed radius.

In a second analysis, a normal distributed random error with a standard deviation of $1\,m\,s^{-1}$ is added to the synthetic radial velocities, which represents the measurement error of radars. Additionally, COSMO-DE information about water content is used to restrict the data to areas where rainfall is considered (see section 2). Again, the data are interpolated to the Cartesian grid using the fixed and the variable radiuses of influence.

Figure 10d shows the results for the same configuration as used in Fig. 10c, but for the restricted data with added simulated error. Luckily, the data for this date and altitude level are not restricted much due to the overall high water content. Because of the strong smoothing, the added random error almost does not affect the interpolated wind field. The RMSE and the MAE for this field are shown in Fig. 11b. For the restricted data, the variable radius of influence reduces the mean RMSE by 43.9% and the MAE by 36.6%.

In this evaluation the focus is on the horizontal radius of influence. As already mentioned, the vertical radius of influence is also of great importance. It is set to half the beamwidth that was found to be the best compromise between data coverage and interpolation error. Increasing the vertical radius of influence led to higher interpolation errors (error plots can be found in appendix C). There exist other publications where
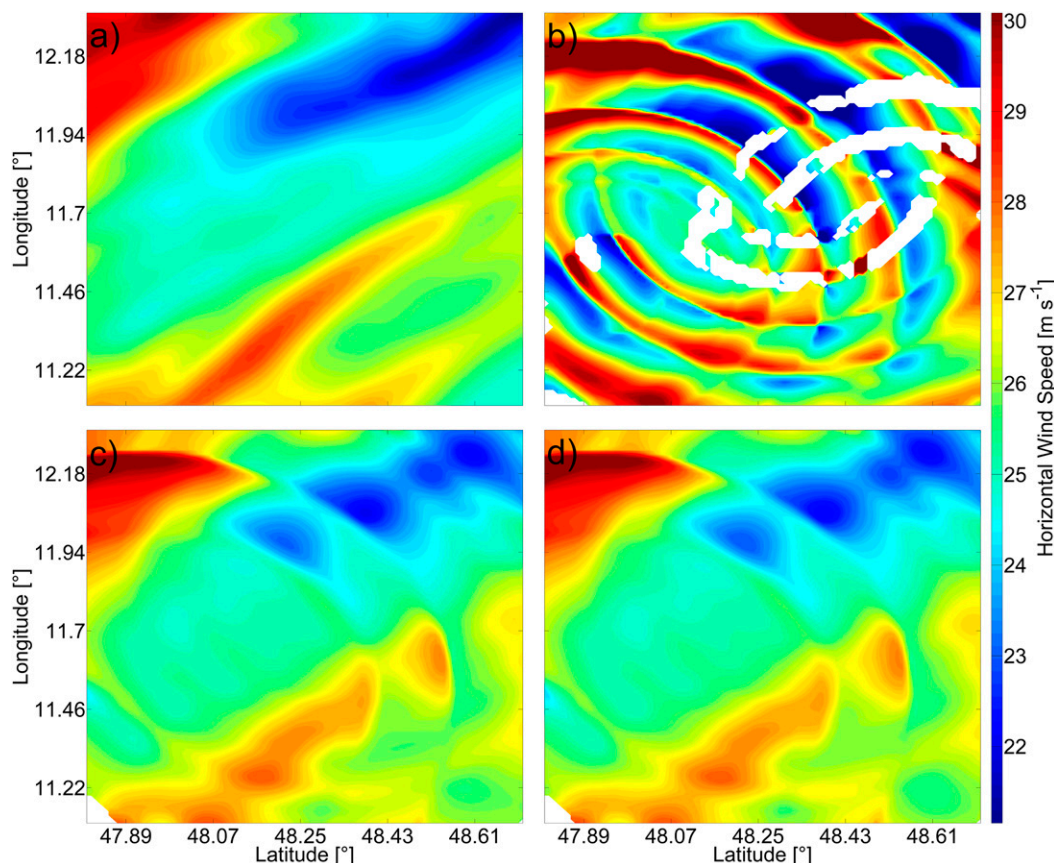
FIG. 10. Magnitude of horizontal wind vector **v** (m s^{-1}) in the domain of interest at 1130 UTC 17 Jan 2014. (a) The COSMO-DE analysis. (b) Interpolated magnitude with a fixed horizontal influence radius. (c) As in (b), but with a variable radius of influence depending on the vertical gradient of the horizontal wind speed. (d) As in (c), but for simulated data with added error.

the vertical radius of influence is set greater. Bousquet et al. (2008) used a whole beamwidth; Zhang et al. (2005) used distance between two adjacent tilts and found a reduction in interpolation errors due to this "vertical interpolation." They analyzed one convective and one stratiform reflectivity field. For the stratiform case, additional horizontal interpolation between neighboring beams improved the results further. It is easy understandable, as this fills data gaps without blurring information in the wrong places. For the convective case, the additional horizontal interpolation led to artifacts in the results but the vertical interpolation improved the result—that is also obvious, as for reflectivity, even in the convective case the vertical gradient was small. For wind the vertical gradient can be much higher and vertical interpolation is not fruitful. To not lose information or skip wind shear for the presented radar configuration, a smaller vertical search radius is preferred. Existing data gaps can be filled later on with the use of additional methods, like three-dimensional variational data

assimilation (3DVAR) with, for example, the mass continuity equation.

The lookup table (Table B1) shows that for the different combinations of altitude level and vertical gradient, the optimal radius of influence is often found to be greater than 3 km. This generates a smoothing compared to the reference case. As a result the error produced by a vertical gradient or erroneous data is reduced at the cost of a loss of small-scale information, which is needed to resolve small convective cells. In the simplified case of a wind field with a strong horizontal gradient but no vertical gradient, a higher smoothing would increase the interpolation error. Therefore, a second method for reducing error due to the vertical gradient is presented.

c. Including vertical wind gradient to interpolation

If the horizontal gradient in the wind vector is small, then the change in the radial velocity along the beam can be directly used to estimate the vertical wind gradient. For the interpolation of a data point to the Cartesian grid at a specific altitude level, the measurement is
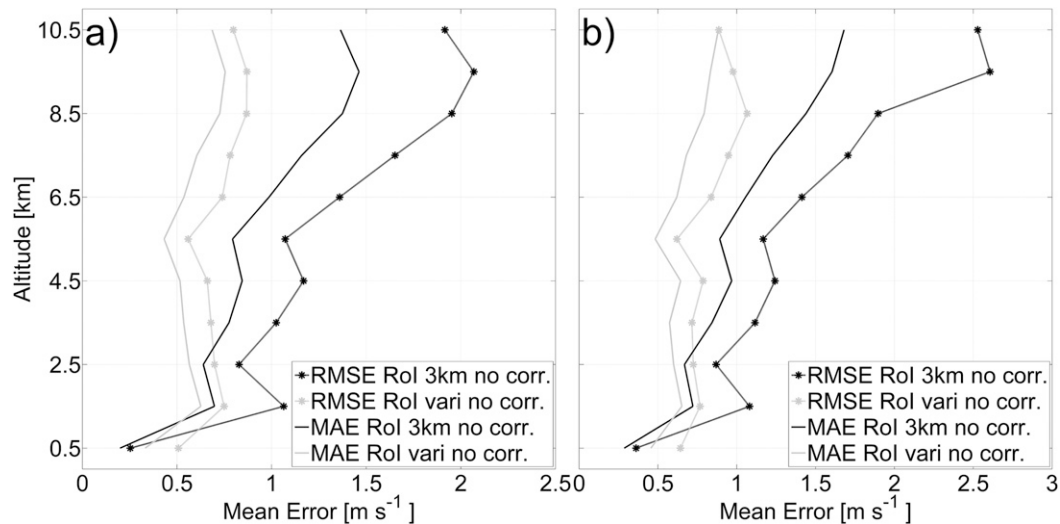
FIG. 11. RMSE (dashed line) and MAE (solid line) as a function of altitude level. All analyzed cases are considered: a fixed horizontal radius of influence of 3 km (black lines), and a variable horizontal radius of influence depending on the vertical wind gradient and the current altitude level (gray lines). (a) The full data coverage is used without any restrictions or added error. (b) The restricted dataset is used with an added simulated error.

corrected according to the estimated vertical gradient with the simple formula

$$\tilde{\mathbf{v}}_r = \mathbf{v}_r + \frac{\partial \mathbf{v}_r}{\partial z} \Delta z.$$

Here $\tilde{\mathbf{v}}_r$ is the corrected radial velocity, $\mathbf{v}_r$ is the measured radial velocity, and Δz is the vertical distance between the measurement and grid point. The vertical gradient $\partial \mathbf{v}_r / \partial z$ is calculated as a least squares fit of all previous values within a range of 5 km in the horizontal.

Figure 12 shows the interpolation for the same wind field as in section 3b but with the correction of the radial velocity with the vertical gradient. As can be seen the interpolation error is reduced—that applies to the analysis with the full data coverage (Fig. 12a) and to the analysis with the restricted data with added error (Fig. 12b). Figure 13 shows how the RMSE and the MAE of the interpolation of 16 different wind fields are diminished for the analyses with the correction (gray line) compared to the analyses without the correction (black line). In Fig. 13a the full synthetic data coverage is used and the data are not influenced by an added error.

The same analyses are made for the restricted synthetic data with an added random error as in section 3b. Results are shown in Figs. 12b and 13b. Compared to the case without restriction and added error to the data, the interpolated RMSE is reduced less (11.7% compared to 30.72%); this is mainly caused by some outliers in high altitudes. The MAE is reduced by 34.94% compared to 44.33%. For both cases (full data and restricted data), the reduction of the MAE is stronger than the reduction

of the RMSE, which suggests that there are a few outliers with huge errors and an average with small errors. This can be attributed to the estimation of the vertical gradient, which can be inaccurate, especially when the vertical gradient is heterogeneous or the horizontal gradient is unexpectedly high. The effect can be seen in the contour plot of the analyzed wind field (Figs. 12a and 12b) and is stronger for the restricted data, as here in addition the estimation of the vertical gradient is more complicated because the data are noisier.

4. Conclusions

We have shown how gaps in radar data coverage in combination with a vertical gradient in wind speed can lead to circular features in the interpolation of radar data, measured in polar coordinates, to Cartesian coordinates. These errors occur independently of the interpolation method, as the vertical gradient is projected onto the horizontal due to missing information above and below a radar beam. In our study we used a direct interpolation method with a weighted least squares fit. Using an indirect interpolation—for example, by minimizing a cost function with a term measuring the data fit and the additional use of other terms representing smoothing or low-pass filtering—might reduce the problem through higher smoothing, but it has the disadvantage that the whole wind field is smoothed, leading to a loss of small-scale information.

Shortages in data coverage arise especially for operational weather radars, as they use a reduced number of
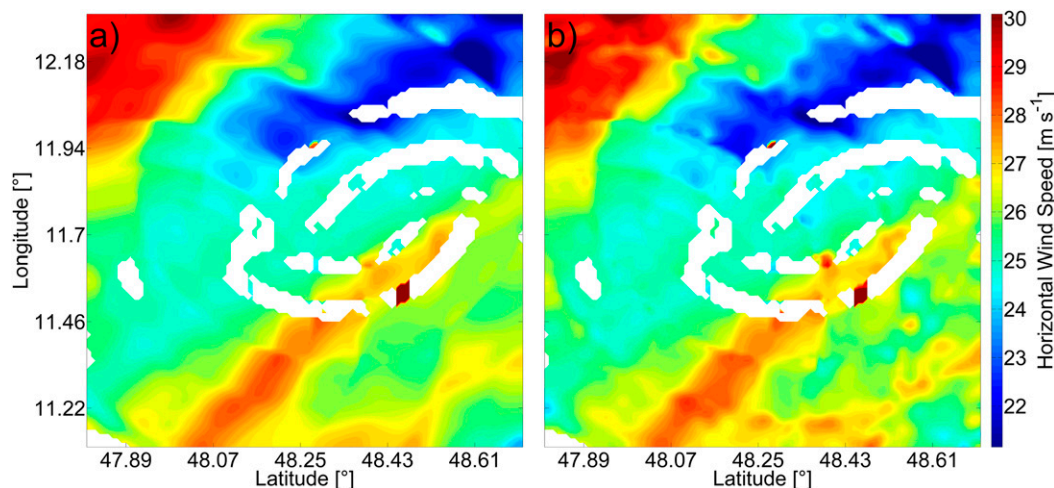
FIG. 12. Magnitude of horizontal wind vector **v** (m s^{-1}) in the domain of interest at 1130 UTC 17 Jan 2014. Interpolation is done with a fixed horizontal radius of influence of 3 km and with the data corrected using the vertical gradient. (a) For simulated data with full data coverage without error. (b) For restricted data with added error.

elevation angles to fill the volume rapidly. Improvements can be found for radar networks that limit their regular volume scans to low elevation angles with small steps between two adjacent tilts.

The problem of sparse data coverage due to the anisotropic character of radar data density is already addressed in other publications but with the focus on reflectivity (see, e.g., Zhang et al. 2005). The suggested solution of increasing the vertical radius of influence cannot be used for the interpolation of wind by default, as there exist essential vertical gradient—for example, due to wind shear—that should not be smoothed out.

To tackle the wind speed interpolation problem for the radar configuration covering the Munich airport, we generated synthetic radar data for the three radars shown in Fig. 3. The analysis volume has a size of $100 \times 100 \times 10 \text{ km}^3$ and a resolution of $1 \times 1 \times 1 \text{ km}^3$.

We have shown that a fixed interpolation radius of 3 km, as proposed in many studies for the analysis with the French radar network (Bousquet and Chong 1998), can lead to great errors in our configuration, since the ellipses of influence of beams with different elevation angles do not overlap. Enlarging the radius of influence is generally not recommended, as this leads to a
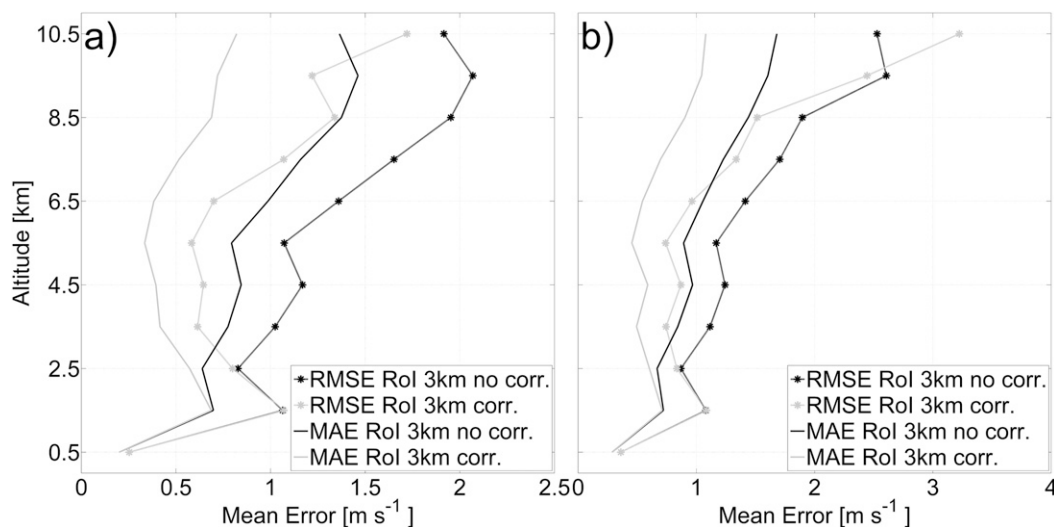

FIG. 13. As in Fig. 11, but for interpolation with ''untreated'' radial velocities (black lines) and with corrected radial velocities with the vertical gradient (gray lines).

TABLE A1. Statistics of the horizontal wind speed $(u^2 + v^2)^{1/2}$ for the analyzed COSMO-DE Model output wind fields. Given are mean value, standard deviation, % quantile (q95), and minimum and maximum values.

Date (2014)	Time (UTC)	Mean (m s^{-1})	Std dev (m s^{-1})	q95 (m s^{-1})	Min (m s^{-1})	Max (m s^{-1})
14 Jan	1300	18.3	10.2	32.2	0	37
17 Jan	1130	27.5	15	50.3	1.3	55
21 Jan	1130	5	3.8	11.5	0	15.3
21 Feb	1130	15.1	5.3	23.8	3.3	27.1
8 Apr	1000	18.8	3.4	24.5	9.4	28.6
7 May	0830	23.7	8.4	39.3	6.1	40.5
2 Jul	1300	15.8	10.8	33.6	0	36
8 Jul	1300	13.9	5	20.5	0.9	24.1
9 Jul	1000	11.1	6.3	22.6	0	29.7
21 Jul	1300	13.6	6	26.3	2	30.6
11 Aug	1000	22.5	12.3	42	0.1	45.1
13 Aug	1000	22.8	12.5	45.5	0.2	56.7
12 Sep	1130	17.2	9.6	31.6	0	35.1
6 Oct	1300	26.6	16.7	45.3	0	48.4
18 Oct	1130	7.6	3.9	13.5	0	17.7
16 Dec	1430	14.4	5.1	22.2	3.9	24.1

smoothing of the interpolated field. But, as the interpolation error depends on the vertical gradient, the vertical gradient can be used to find an optimal radius of influence. Therefore, we generated synthetic radar data from simplified synthetic wind fields with easy structure (see Fig. 5) and different vertical gradients that we interpolated to a predefined Cartesian grid with an increasing radius of influence. The resulting interpolation errors were used to create a lookup table for the horizontal interpolation radius as a function of altitude and mean vertical gradient (section 3b).

The new method has been evaluated with 16 wind fields generated by the COSMO-DE Model. We created two different datasets: The first with the fullest possible data coverage and without an added measurement error, and the second with a restriction of the data to areas with high water content (rainfall is assumed) and with an added normal-distributed random error with a standard deviation of 1 m s^{-1}. With the use of the optimal radius of influence, the interpolation MAE is reduced by 44.9% for the first dataset and by 43.9% for the second one. Nevertheless, it has to be mentioned that the optimal radius of influence is often found to be greater than 3 km, which leads to the abovementioned smoothing and a loss of small-scale information.

Therefore, we presented a second method to deal with vertical gradients in the data. Provided that the horizontal gradient is insignificant compared to the vertical gradient, the vertical gradient can be estimated along the radar ray with a least squares fit. The measurement is then corrected with the estimated gradient and the vertical distance to the corresponding grid point. This

TABLE A2. As in Table A1, but for vertical gradient of the horizontal wind speed.

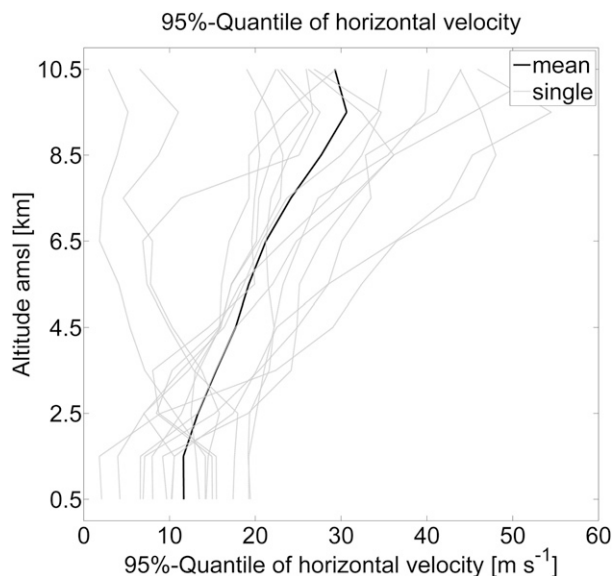| Date (2014)	Time (UTC)	Mean (m s^{-1} km^{-1})	Std dev (m s^{-1} km^{-1})	q95 (m s^{-1} km^{-1})	Max (m s^{-1} km^{-1})
14 Jan	1300	5.9	3.7	11.7	23.9
17 Jan	1130	7.5	6.1	21.6	32.7
21 Jan	1130	3.3	2.7	9.6	13.7
21 Feb	1130	3.6	2.5	9.3	13.8
8 Apr	1000	4	3.5	10.6	35.5
7 May	0830	4.3	2.7	9.3	15.8
2 Jul	1300	4.6	2.9	9.9	14.9
8 Jul	1300	4.8	3.4	11.4	21.1
9 Jul	1000	6.2	5.5	18.4	29.9
21 Jul	1300	5.6	3.4	11.6	20
11 Aug	1000	5.9	3.9	13.5	23.2
13 Aug	1000	5.8	4.5	14.6	31.6
12 Sep	1130	6.4	4.3	16.5	26.6
6 Nov	1300	6	4.1	15	21.4
18 Nov	1130	6.7	7.9	26.8	42.9
16 Dec	1430	3.4	2.3	8.4	13.7

FIG. A1. The 95% quantile of horizontal wind speed for the analyzed COSMO-DE Model output wind fields; the mean 95% quantile is shown (black line).

method works very well in the case of no measurement error, reducing the mean interpolation error by 44.3%. Limitations are an unstable vertical gradient or a large horizontal gradient, which can occur in convective situations. For the synthetic data with an added measurement error, the mean interpolation error is reduced by 34.9%, as measurement errors can affect the estimation of the vertical gradient additionally. Combining the two methods (not shown) will slightly further improve the performance. The MAE is reduced by 48.8% for the first dataset and by 46.0% for the second dataset. Though, to preserve small-scale features we recommend correcting only the radial velocity with the vertical gradient rather than additionally using the optimal radius of influence.

In the presented cases, the RMSE is less reduced than the MAE, indicating large outliers in the analyses due to a wrong estimation of the vertical gradient of the field. To overcome this we suggest a multigrid interpolation procedure, where the data are interpolated to a number of grids with successively higher resolution (results not shown). Values that differ from the interpolated field at the coarse grid by more than a defined limit will not be included in the analysis. Besides, other methods for estimating the vertical gradient can be considered. Especially in lower altitudes, where the ascent of a beam is small, information from adjacent tilts can be used to estimate the gradient. The interpolation of measurements to a predefined grid is a difficult task that should be set up depending on the specific radar configuration. The interpolation procedure itself is not done by a simple weighting of each
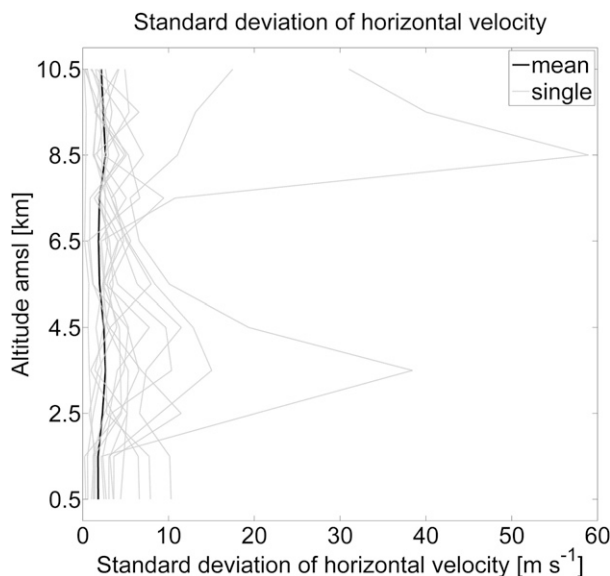

FIG. A2. As in Fig. A1, but for the variance.

data point, as incorrectly gridded values can worsen the result; nevertheless, it can be corrected with additional information. The advantage of using radar data is the large number of data points from which additional information can be extracted. Especially with the second method introduced in this paper, which differs from all existing methods, we presented a method that benefits from such additional information. This method, which is unique and easy to implement, will help improve the analysis of operational weather radar.

APPENDIX A

Analyzed COSMO-DE Model Output Wind Fields

Tables A1 and A2 and Figs. A1–A4 provide some statistics for the wind situation from analyzed wind fields for comparison.

APPENDIX B

Lookup Table for the Variable Radius of Influence

Table B1 provides a lookup table for the variable radius of influence (km) as a function of the altitude level and the vertical gradient. The values for the optimal radius of influence are found by analyzing the interpolation error from idealized wind fields with different
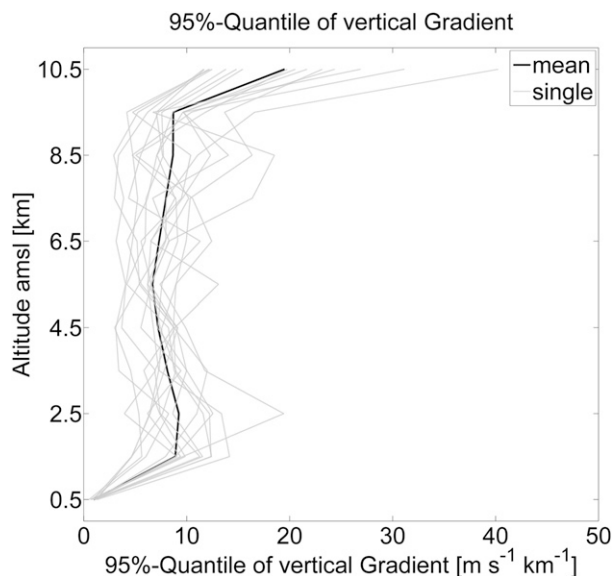
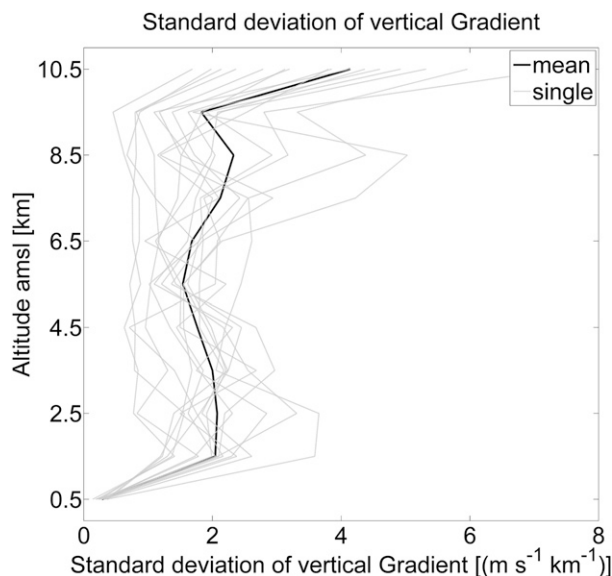FIG. A3. As in Fig. A1, but for the vertical gradient of the horizontal wind speed.

FIG. A4. As in Fig. A3, but for the standard deviation of the vertical gradient.

vertical gradients. The optimal radius of influence is the smallest radius of influence, so that the mean interpolation error at one altitude level decreases below $0.5\,\mathrm{m\,s^{-1}}$.

APPENDIX C

Error Plots for the Analysis with Greater Vertical Radius of Influence

Some publications suggest a vertical radius of influence that is greater than half the beamwidth as is used in this work (e.g., Zhang et al. 2011; Bousquet et al. 2008). Zhang et al. (2005) discussed the use of adjacent tilts for the interpolation of reflectivity data, what they called vertical interpolation. To evaluate the possible benefit of using the distance between adjacent tilts as the vertical radius of influence, we interpolated the data with this method. The horizontal radius of influence is set to 3 km.

Figure C1 shows the RMSE and the MAE for all analyzed cases at altitude levels from 0.5 to $10.5\,\mathrm{m\,s^{-1}}$ and for a vertical radius of influence as a function of half the beamwidth (black line) and a vertical radius of influence depending on the distance between adjacent tilts (gray line). For Fig. C1(a) the full data coverage is used without any restrictions or added error, whereas for Fig. C1(b) the restricted dataset is used with an added simulated error.

In low altitudes there is little difference between the two methods because they have a similar vertical radius of influence in absolute size from the altitude where the cone of their lowest elevation scans overlap (1–2 km above ground). In higher altitudes, using the distance between two adjacent tilts leads to much greater

TABLE B1. Lookup table for the variable radius of influence (km) as a function of the altitude level and the vertical gradient.

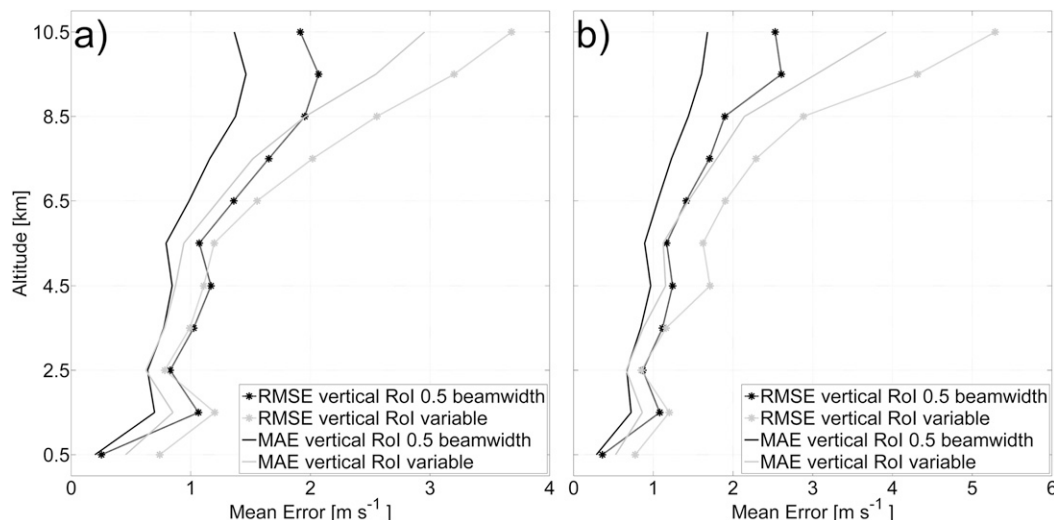| Gradient (m s^{-1} km^{-1})	Altitude MSL (km)										
	0.5	1.5	2.5	3.5	4.5	5.5	6.5	7.5	8.5	9.5	10.5
0	3	3	3	3	3	3	3	3	3	3	3
1	4	4	4	4	4	6	8	10	10	10	10
2	4	4	4	4	4	7	9	10	10	10	10
3	4	4	4	6	7	7	9	10	10	10	12
4	4	4	4	6	7	8	9	10	10	11	12
5	4	4	4	6	7	8	9	10	10	11	12
6	4	4	4	6	7	8	9	10	11	12	12
7	4	4	4	6	7	8	9	10	11	12	12
8	4	4	4	6	7	8	9	10	11	12	12
9	4	4	4	6	7	8	9	10	11	12	12
≥10	4	4	4	6	7	10	11	11	11	12	12

FIG. C1. RMSE (dashed line) and MAE (solid line) as a function of altitude level. All analyzed cases are considered: a vertical radius of influence as a function of half the beamwidth (black lines), and a vertical radius of influence depending on the distance between adjacent tilts (gray lines). (a) The full data coverage is used without any restrictions or added error. (b) The restricted dataset is used with added simulated error.

vertical radius of influence, and the error increases. This is caused by existing vertical gradients and too high smoothing.

REFERENCES

Armijo, L., 1969: A theory for the determination of wind and precipitation velocities with Doppler radars. *J. Atmos. Sci.*, **26**, 570–573, doi:10.1175/1520-0469(1969)026<0570: ATFTDO>2.0.CO;2.

Askelson, M. A., J.-P. Aubagnac, and J. M. Straka, 2000: An adaptation of the Barnes filter applied to the objective analysis of radar data. *Mon. Wea. Rev.*, **128**, 3050–3082, doi:10.1175/1520-0493(2000)128<3050:AAOTBF>2.0.CO;2.

Baldauf, M., A. Seifert, J. Förstner, D. Majewski, M. Raschendorfer, and T. Reinhardt, 2011: Operational convective-scale numerical weather prediction with the COSMO model: Description and sensitivities. *Mon. Wea. Rev.*, **139**, 3887–3905, doi:10.1175/MWR-D-10-05013.1.

Beck, J., M. Nuret, and O. Bousquet, 2014: Model wind field forecast verification using multiple-Doppler syntheses from a national radar network. *Wea. Forecasting*, **29**, 331–348, doi:10.1175/WAF-D-13-00068.1.

Bousquet, O., and M. Chong, 1998: A multiple-Doppler synthesis and continuity adjustment technique (MUSCAT) to recover wind components from Doppler radar measurements. *J. Atmos. Oceanic Technol.*, **15**, 343–359, doi:10.1175/1520-0426(1998)015<0343:AMDSAC>2.0.CO;2.

——, and P. Tabary, 2014: Development of a nationwide real-time 3-D wind and reflectivity radar composite in France. *Quart. J. Roy. Meteor. Soc.*, **140**, 611–625, doi:10.1002/qj.2163.

——, ——, and J. Parent du Châtelet, 2008: Operational multiple-Doppler wind retrieval inferred from long-range radial velocity measurements. *J. Appl. Meteor. Climatol.*, **47**, 2929–2945, doi:10.1175/2008JAMC1878.1.

——, J. Delanoë, and S. Bielli, 2016: Evaluation of 3D wind observations inferred from the analysis of airborne and ground-based radars during HyMeX SOP-1. *Quart. J. Roy. Meteor. Soc.*, **142**, 86–94, doi:10.1002/qj.2710.

Cressman, G. P., 1959: An operational objective analysis system. *Mon. Wea. Rev.*, **87**, 367–374, doi:10.1175/1520-0493(1959)087<0367: AOOAS>2.0.CO;2.

Easterbrook, C. C., 1975: Estimating horizontal wind fields by two-dimensional curve fitting of single Doppler radar measurements. Preprints, *16th Conf. on Radar Meteorology*, Houston, TX, Amer. Meteor. Soc., 214–219.

Gao, J., M. Xue, A. Shapiro, and K. K. Droegemeier, 1999: A variational method for the analysis of three-dimensional wind fields from two Doppler radars. *Mon. Wea. Rev.*, **127**, 2128–2142, doi:10.1175/1520-0493(1999)127<2128:AVMFTA>2.0.CO;2.

Helmert, K., and Coauthors, 2014: DWDs new radar network and post-processing algorithm chain. Extended Abstracts, *Eighth European Conf. on Radar in Meteorology and Hydrology*, Garmisch-Patenkirchen, Germany, ERAD, 4.4. [Available online at http://www.pa.op.dlr.de/erad2014/programme/ExtendedAbstracts/237_Helmert.pdf.]

Joss, J., and A. Waldvogel, 1970: A method to improve the accuracy of radar-measured amounts of precipitation. Preprints, *14th Conf. on Radar Meteorology*, Tucson, AZ, Amer. Meteor. Soc., 237–238.

Kessler, E., 1995: On the continuity and distribution of water substance in atmospheric circulations. *Atmos. Res.*, **38**, 109–145, doi:10.1016/0169-8095(94)00090-Z.

Lakshmanan, V., T. Smith, K. Hondl, G. J. Stumpf, and A. Witt, 2006: A real-time, three-dimensional, rapidly updating, heterogeneous radar merger technique for reflectivity, velocity, and derived products. *Wea. Forecasting*, **21**, 802–823, doi:10.1175/WAF942.1.

Laroche, S., and I. Zawadzki, 1994: A variational analysis method for retrieval of three-dimensional wind field from single-Doppler radar data. *J. Atmos. Sci.*, **51**, 2664–2682, doi:10.1175/1520-0469(1994)051<2664:AVAMFR>2.0.CO;2.

Lhermitte, R. M., 1966: Application of pulse Doppler radar technique to meteorology. *Bull. Amer. Meteor. Soc.*, **47**, 703–711.

López Carrillo, C., and D. Raymond, 2011: Retrieval of three-dimensional wind fields from Doppler radar data using an efficient two-step approach. *Atmos. Meas. Tech.*, **4**, 2717–2733, doi:10.5194/amt-4-2717-2011.

Miller, L., and R. Strauch, 1974: A dual Doppler radar method for the determination of wind velocities within precipitating weather systems. *Remote Sens. Environ.*, **3**, 219–235, doi:10.1016/0034-4257(74)90044-3.

Nash, S. G., and A. Sofer, 1996: *Linear and Nonlinear Programming.* McGraw-Hill, 692 pp.

Probert-Jones, J., 1960: Meteorological use of pulsed Doppler radar. *Nature*, **186**, 271–273, doi:10.1038/186271a0.

Protat, A., and I. Zawadzki, 1999: A variational method for real-time retrieval of three-dimensional wind field from multiple-Doppler bistatic radar network data. *J. Atmos. Oceanic Technol.*, **16**, 432–449, doi:10.1175/1520-0426(1999)016<0432:AVMFRT>2.0.CO;2.

Ray, P. S., C. L. Ziegler, W. Bumgarner, and R. J. Serafin, 1980: Single- and multiple-Doppler radar observations of tornadic storms. *Mon. Wea. Rev.*, **108**, 1607–1625, doi:10.1175/1520-0493(1980)108<1607:SAMDRO>2.0.CO;2.

Simonin, D., S. Ballard, and Z. Li, 2014: Doppler radar radial wind assimilation using an hourly cycling 3D-Var with a 1.5 km resolution version of the Met Office Unified Model for nowcasting. *Quart. J. Roy. Meteor. Soc.*, **140**, 2298–2314, doi:10.1002/qj.2298.

Tuttle, J. D., and G. B. Foote, 1990: Determination of the boundary layer airflow from a single Doppler radar. *J. Atmos. Oceanic Technol.*, **7**, 218–232, doi:10.1175/1520-0426(1990)007<0218:DOTBLA>2.0.CO;2.

Van Zadelhoff, G.-J., A. Stoffelen, P. Vachon, J. Wolfe, J. Horstmann, and M. Belmonte Rivas, 2014: Retrieving hurricane wind speeds using cross-polarization C-band measurements. *Atmos. Meas. Tech.*, **7**, 437–449, doi:10.5194/amt-7-437-2014.

Waldteufel, P., and H. Corbin, 1979: On the analysis of single-Doppler radar data. *J. Appl. Meteor.*, **18**, 532–542, doi:10.1175/1520-0450(1979)018<0532:OTAOSD>2.0.CO;2.

Woodhouse, M., A. Hogg, J. Phillips, and R. Sparks, 2013: Interaction between volcanic plumes and wind during the 2010 Eyjafjallajökull eruption, Iceland. *J. Geophys. Res. Solid Earth*, **118**, 92–109, doi:10.1029/2012JB009592.

Zhang, J., K. Howard, and J. Gourley, 2005: Constructing three-dimensional multiple-radar reflectivity mosaics: Examples of convective storms and stratiform rain echoes. *J. Atmos. Oceanic Technol.*, **22**, 30–42, doi:10.1175/JTECH-1689.1.

——, and Coauthors, 2011: National Mosaic and Multi-Sensor QPE (NMQ) system: Description, results, and future plans. *Bull. Amer. Meteor. Soc.*, **92**, 1321–1338, doi:10.1175/2011BAMS-D-11-00047.1.